

Lawrence Berkeley National Laboratory

Recent Work

Title

CRYSTAL STRUCTURE AND MICROSTRUCTURE OF γ -Fe₂O₃ PARTICLES

Permalink

<https://escholarship.org/uc/item/91r0t5tk>

Author

Ho, H.-M.

Publication Date

1985-08-01



Lawrence Berkeley Laboratory

UNIVERSITY OF CALIFORNIA

Materials & Molecular Research Division

CRYSTAL STRUCTURE AND MICROSTRUCTURE
OF γ -Fe₂O₃ PARTICLES

H.-M. Ho
(M.S. Thesis)

August 1985

RECEIVED
LAWRENCE
BERKELEY LABORATORY

JAN 31 1986

LIBRARY AND
DOCUMENTS SECTION

TWO-WEEK LOAN COPY
*This is a Library Circulating Copy
which may be borrowed for two weeks.*



LBL-20570
e.i.2

DISCLAIMER

This document was prepared as an account of work sponsored by the United States Government. While this document is believed to contain correct information, neither the United States Government nor any agency thereof, nor the Regents of the University of California, nor any of their employees, makes any warranty, express or implied, or assumes any legal responsibility for the accuracy, completeness, or usefulness of any information, apparatus, product, or process disclosed, or represents that its use would not infringe privately owned rights. Reference herein to any specific commercial product, process, or service by its trade name, trademark, manufacturer, or otherwise, does not necessarily constitute or imply its endorsement, recommendation, or favoring by the United States Government or any agency thereof, or the Regents of the University of California. The views and opinions of authors expressed herein do not necessarily state or reflect those of the United States Government or any agency thereof or the Regents of the University of California.

**CRYSTAL STRUCTURE AND MICROSTRUCTURE
OF γ -Fe₂O₃ PARTICLES**

by

**Huei-Min Ho
(M. S. Thesis)**

**Department of Materials Science and Mineral Engineering
Materials and Molecular Research Division
Lawrence Berkeley Laboratory
University of California at Berkeley
Berkeley, California 94720**

August 1985

**CRYSTAL STRUCTURE AND MICROSTRUCTURE
OF γ -Fe₂O₃ PARTICLES**

Huei-Min Ho

**Materials and Molecular Research Division
Lawrence Berkeley Laboratory
and
Department of Materials Science and Mineral Engineering
University of California, Berkeley, California 94720**

ABSTRACT

The structure and microstructure of γ -Fe₂O₃ particles used in magnetic recording media have been analyzed by convergent beam electron diffraction and conventional transmission electron microscopy.

Convergent beam electron diffraction results show that γ -Fe₂O₃ particles have a primitive lattice with an m3m point group and a cubic superstructure with lattice parameter approximately equal to three times the lattice parameter of the magnetite structure. This superlattice is a result of cation vacancy ordering. An order-disorder transition of the structure is observed in the electron microscope and is believed to be caused by electron radiation-enhanced diffusion.

Transmission electron microscopy results show that these particles are single crystals, and hence the theory that polycrystallinity is the cause of the discrepancy in coercivity between the experimental and theoretical values cannot be true. The results also show that the long axis directions of the particles are along low order directions (e.g. $\langle 100 \rangle$, $\langle 110 \rangle$, $\langle 111 \rangle$ etc.) with about 30% along $\langle 110 \rangle$ which are the easy directions of the material.

CRYSTAL STRUCTURE AND MICROSTRUCTURE
OF γ -Fe₂O₃ PARTICLES

CONTENTS

	<u>Page</u>
I. Introduction	1
II. Background Studies	3
A. Magnetic Properties	3
1. Magnetization	3
2. Coercivity	4
B. Previous Studies	7
1. Structure and vacancy distribution	7
2. Microstructure	8
III. Experimental Procedures	10
A. Specimen Preparation	10
B. Transmission Electron Microscopy and Convergent Beam Electron Diffraction	11
IV. Experimental Results	13
A. Structural Studies	13
B. Microstructural Studies	16
c. Non-Magnetic Properties	17

V. Discussion	19
VI. Conclusion	23
Acknowledgements	25
References	26
Figure Captions	29
Figures	32
Tables	50

I. Introduction

Magnetic recording is the most widely used method of storing information today, mainly due to the fact that large amounts of information can be stored cheaply and reliably on an erasable and rewritable medium. Magnetic recording takes three forms to store information: magnetic tapes, floppy disks, and hard disks, but in general the magnetic materials used are the same.

Fig. 1 shows the scanning electron microscope (SEM) images of commercial audio tapes of different grade. These acicular particles are made of $\gamma\text{-Fe}_2\text{O}_3$ which was the earliest material used for magnetic tapes and today it is still the most widely used magnetic material for disks and tapes. $\gamma\text{-Fe}_2\text{O}_3$ is commonly prepared via the conversion of αFeOOH or γFeOOH to Fe_3O_4 ^{1,2}, by heating and reduction, followed by oxidation of the Fe_3O_4 to $\gamma\text{-Fe}_2\text{O}_3$. Fe_3O_4 , which has a cubic inverse spinel structure, converts to $\gamma\text{-Fe}_2\text{O}_3$ by removing $8/3$ Fe ions per unit cell.

Because of its application as magnetic recording media, the structure and microstructure of $\gamma\text{-Fe}_2\text{O}_3$ materials have been studied by many investigators. However, due to (1) the fact that the structure contains large amounts of cation vacancies so that it is sensitive to the environment, (2) the small particle sizes, and

(3) the difficulty in growing single crystals for X-ray determination, unambiguous result for the structure and microstructure have not yet been obtained.

In this study, γ -Fe₂O₃ acicular particles were examined by transmission electron microscopy (TEM) and convergent beam electron diffraction (CBED) to allow examination of individual particles and to determine their crystal structure and microstructure directly. Several new results concerning the structure and microstructure of γ -Fe₂O₃ have been obtained. Some non-magnetic properties, which were evident in observations of commercial tapes, are also discussed.

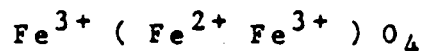
II. Background Studies

(A) Magnetic Properties

The desirable magnetic properties of a magnetic recording media are (1) A high saturation magnetization and a high remanent-to-saturation magnetization ratio (i.e. squareness, $S = M_r/M_s$ where M_r and M_s are remanent and saturation magnetization, respectively). (2) A coercivity which is high enough to withstand the demagnetization due to the recording and reproducing losses but low enough to allow relatively easy recording and erasure.

(1) Magnetization

$\gamma\text{-Fe}_2\text{O}_3$ is commonly obtained from Fe_3O_4 by oxidation. Magnetite (Fe_3O_4) is a ferrimagnetic material which, like ferromagnetics, exhibit a substantial spontaneous magnetization at room temperature and the phenomenon of magnetic saturation and hysteresis. Magnetite has an inverse spinel structure. Fig. 2 shows the spinel structure³, in which the large oxygen ions are packed in a face-centered cubic arrangement and the smaller iron ions occupy the space between them. In the case of magnetite there are 16 out of 32 octahedral or B sites and 8 out of 64 tetrahedral or A sites occupied by the iron ions, and the structure can be represented by



where the brackets indicate B sites.

Upon oxidation to $\gamma\text{-Fe}_2\text{O}_3$ the oxygen lattice of Magnetite remains practically unchanged. But due to the charge neutrality, $8/3$ Fe ions per unit cell are removed resulting in a defective structure. The structure of $\gamma\text{-Fe}_2\text{O}_3$ can be magnetically expressed by $\text{Fe}^{3+}_8 (\text{Fe}^{3+}_{13\frac{1}{3}} \text{X}_{8/3}) \text{O}_{32}$ where X represents cation vacancies. The net magnetic moment is the result of the imbalance between these two oppositely oriented iron sites. Thus, the magnetic moment can be calculated as 2.5 Bohr magnetons per molecule which has been shown to be in good agreement with the experimental values⁴.

While saturation magnetization is an intrinsic property, remanent magnetization is an extrinsic property. It depends on the particle alignment as well as on their shape and size⁵. Therefore, processing factors which affect particle alignment, shape and size distribution etc. are also important in determining the performance of magnetic materials.

(2) Coercivity

The coercivity of fine particles is primarily due to the shape anisotropy and/or crystal anisotropy. In any crystal, an energy is required to force the magnetization vector M_s to point in a non-easy direction. This crystal anisotropy energy E can be expressed by⁴

$$E = K_0 + K_1(\alpha_1^2 \alpha_2^2 + \alpha_2^2 \alpha_3^2 + \alpha_3^2 \alpha_1^2) + K_2(\alpha_1^2 \alpha_2^2 \alpha_3^2) + \dots$$

where $\alpha_1, \alpha_2, \alpha_3$ are the cosines of angles a, b, c that M_s makes with the crystal axes and K_1 is the dominant factor concerning the change in the energy E when the M_s vector rotates from one direction to another.

In the case of $\gamma\text{-Fe}_2\text{O}_3$, because of its small K_1 anisotropy constant value⁶ crystal anisotropy is relatively unimportant. It has been reported⁷ that crystal anisotropy accounts for approximately 1/3 the observed room temperature coercivity. Since the easy axis of the material has been determined⁶ to be $\langle 110 \rangle$, crystal anisotropy may be increased by having the long axes of the particles along $\langle 110 \rangle$ directions.

Assuming a prolate spheroid shaped material, shape anisotropy can be expressed⁸ by

$$H = (N_a - N_c) M_s$$

where N_a and N_c are demagnetizing coefficients along the a and c axes of a prolate spheroid respectively.

Assuming very long particles with $N_c = 0$, $N_a = 2\pi$ and $M_s = 400 \text{ emu/cm}^3$, the coercivity of $\gamma\text{-Fe}_2\text{O}_3$ particles is calculated to be approximately equal to 2500 Oe ⁹, which is much larger than the experimental value (about 300 Oe).

This discrepancy between the experimental and the theoretical values has been discussed by many investigators^{10,11}. Today, among the proposed models, it is

believed that chain-of-sphere model, in which the magnetization on alternate spheres rotates in opposite directions, describes the reversal behavior of $\gamma\text{-Fe}_2\text{O}_3$ particles most satisfactorily. Hence, the microstructure of the particles has been interpreted to be polycrystalline, and composed of magnetically interacting crystallites along the long axis. It has been assumed that each crystallite is a single domain and that the spins in each one reverse coherently. The magnetostatic coupling between two crystallites causes the pair to have a uniaxial anisotropy with an easy axis along the long axis of the particle.

(B) Previous Results

(1) Structure and vacancy distribution

This topic was first studied by Hägg¹² and Verwey¹³ independently using X-ray diffraction powder data. They pointed out that γ -Fe₂O₃ had the same inverse spinel structure as magnetite, but with cation vacancies which distribute uniformly in the cation sites and the resulting space group remains Fd3m. From the measurement of the saturation magnetization, Néel¹⁴ pointed out that cation vacancies are distributed only over the 16d cation sites.

Ferguson and Haas¹⁵ studied the vacancy distribution by neutron diffraction and their work supported the model of preferential distribution of vacancies in the octahedral sites only. Van Oosterhout and Rooijmans¹⁶ and other investigators (Braun¹⁷, Haul and Schoon¹⁸, and Chaudron¹⁹) found many non-magnetite extra lines in the X-ray powder pattern. They attributed these lines to the formation of a superstructure, due to ordering of cation vacancies.

The structure was interpreted as tetragonal with $c/a = 3$ and space group $P4_1$ by Van Oosterhout and Rooijmans¹⁶. It was reported to be similar to the ordered phase in lithium ferrite with space group $P4_132$ (or $P4_332$) by Braun¹⁷. Ueda and Hase²⁰ concluded from their X-ray

and neutron diffraction data that the vacancies can occupy only four of the 16d sites. In contrast to the above reported results, Takei and Chiba⁶ prepared epitaxial single crystal films of $\gamma\text{-Fe}_2\text{O}_3$ which showed no such ordered array of vacancies. Recently, from their X-ray and electron diffraction results of a polyhedral crystal, Boudeulle *et. al.*²¹ concluded that the vacancy ordering depends on the preparative conditions and suggested that the vacancy distribution either results in noncubic symmetry or leads to a cubic superstructure with a threefold unit cell.

(2) Microstructure

As discussed in section II (A), there are two features in the microstructure that are important concerning the magnetic properties: (1) The long axis direction of the particles, is it parallel to the easy direction? (2) Are the particles single crystals or polycrystalline?

Discrepancies also exist in the literature concerning these two features in the $\gamma\text{-Fe}_2\text{O}_3$ acicular particles. Osmond²² reported that the particles were composed of small crystallites which had their needle axis along $\langle 111 \rangle$ directions. Campbell²³ concluded the long axis to be any low order direction. Hurt *et. al.*²⁴ found that most of the particles were polycrystalline and the needle axis was $\langle 110 \rangle$ in single crystals.

Gustard and Vriend²⁵ reported that 40% by volume of their particles had $\langle 110 \rangle$ direction in the long axis. From the argument of the topotactic transformations and the direct determination using selected area electron diffraction, Van Oosterhout²⁶ reported that the long axis directions are along $\langle 110 \rangle$ directions only. Recently, Bate²⁷ concluded that this confusion concerning the orientation of the long axis arose because of different preparation conditions.

III. Experimental Procedures

(A) Specimen Preparation

In this study, two commercial $\gamma\text{-Fe}_2\text{O}_3$ samples from different sources²⁸ were obtained.

(a) Audio tape sample

The plastic substrate of the audio tape was first removed in an acetone solution. Samples were prepared by ion milling the magnetic coating, after being mounted on a electron microscope grid, until thin enough for transmission electron microscopy observation. Ion milling had to be done in a liquid nitrogen cold stage using a 4 to 5 kV accelerated Ar ion beam, impinging on the specimen at 10 degrees to the specimen surface, to avoid radiation damage.

(b) Powder particle sample

Carbon-film coated grids were first prepared by depositing carbon on a mica substrate via carbon evaporation and then, after separation from the substrate, the carbon film was attached to the electron microscope grid. Samples were prepared by dispersing particles in alcohol solution and subsequently deposited on the grids. For samples prepared in this way, ion milling was not required.

(B) TEM and CBED

In structural and microstructural studies, both $\gamma\text{-Fe}_2\text{O}_3$ samples were observed by transmission electron microscopy (TEM) and convergent beam electron diffraction (CBED) techniques. The particles examined were about 0.2 to 0.45 μm in length and had an axial ratio of about 5. Both TEM and CBED were performed in a Philips EM 400 at 100 kV. A liquid nitrogen cold stage was used to acquire sharp CBED patterns and to avoid rapid contamination of the particles under the convergent beam.

CBED was employed mainly for structural studies and the convergent probe size was about 400 \AA in diameter so that the direct observation of individual particles could be done which greatly reduce the difficulty in isolating particles. From a CBED zone axis pattern such as Fig. 3, which is a $\langle 111 \rangle$ zone axis pattern, crystal symmetry information can be obtained by observing the high order Laue zone (HOLZ) symmetry and by observing the internal structure of the zero order discs.

Point group determination²⁹ requires precise examination of the diffraction pattern symmetry and reference to the tables published by Buxton *et. al.*³⁰. Space group determination can be achieved by observing the presence of the so-called line of dynamic absence which occurs in kinematically forbidden reflections and is related to the presence of a screw axis or glide planes³¹.

The long axis direction of the particle can be obtained simply by comparing the bright-field electron microscope image of the particle to the selected area diffraction (SAD) pattern, taking all optical image rotations into account. Table 1 shows the rotation calibration data used in this experiment which was obtained using a MoO_3 single crystal.

The crystalline nature of the $\gamma\text{-Fe}_2\text{O}_3$ particle can be examined by several methods: (1) By taking an SAD from one particle and examining if the pattern is single crystal or not. (2) By probing at different spots along the particle and observing the orientation relationship between different areas of the particle. If the orientation of these diffraction patterns are the same, the particle is single crystal. (3) Utilize dark-field imaging technique. If the whole particle is bright under dark-field imaging conditions, the particle is single crystal.

IV. Experimental Results

(A) Structural Studies

Table 2 is a summary of previous structural studies^{6,12-21}. It is not surprising that these results are not consistent because the techniques employed can only provide average data about the material. In fact, similar X-ray traces were obtained in most of the previous works¹⁶⁻²¹. However, since they were based on different assumptions they were interpreted differently. Among the results, it is generally believed that γ -Fe₂O₃ has a tetragonal structure of $c/a = 3$, where $a = 8.33\text{\AA}$, due to the fractional nature of iron cation vacancies.

X-ray data obtained in the present research were similar to those referenced in the Table 2. As shown in Fig. 4, several non-magnetite extra lines such as 110, 210, 211 etc. were found. These extra lines indicate that a reduction in symmetry from a face-centered cubic lattice to a primitive cubic lattice has occurred. This finding is also supported by electron microdiffraction results, as shown in Fig. 5, in which reflections forbidden by the fcc structure such as 100, 110, 210 etc. are present. For convenience, Fig. 5 is indexed in terms of a Fe₃O₄ unit cell.

Figs. 6 and 7 are primary CBED zone axis patterns of the same specimens as used for X-ray analysis.

In contrast to the previous confusion on its structure, both $\gamma\text{-Fe}_2\text{O}_3$ samples clearly showed the same crystal symmetry. Since the internal structure of the discs cannot be seen, the crystal symmetry must be determined from analysis of the HOLZ symmetry. As shown in Fig. 8, the HOLZ symmetry is more easily resolved when smaller condenser lens apertures are used (e.g. $50\mu\text{m}$).

From Fig. 8, it can be seen that the $\langle 100 \rangle$, $\langle 110 \rangle$ and $\langle 111 \rangle$ zone axis patterns show the 4mm, 2mm and 3m symmetries, respectively. From Table 3 which is published by Buxton *et. al.*³⁰ the observed whole pattern symmetries can be related to possible diffraction groups. For example, 4mm symmetry can be either the 4mm or the $4mm1_R$ diffraction group and 2mm symmetry can be any of the three possible diffraction groups. From the relation between the diffraction groups and the crystal point groups, as shown in Table 4, the point group can be unambiguously determined to be $m\bar{3}m$ which means that vacancies are ordered in such a way that the unit cell remains cubic. This crystal symmetry also rules out all of the space groups proposed by previous investigators^{12,13,16,17}. Due to the small particle size, no structure is visible in the zero order reflections and the space group of the material can not be determined. However, from the knowledge that $\gamma\text{-Fe}_2\text{O}_3$ has a primitive lattice and $m\bar{3}m$ point group, there are only four possible space groups: $Pm\bar{3}m$, $Pm3n$, $Pn\bar{3}m$ and $Pn3n$.

As shown in Fig. 9³², the spacing between layers, H , in the reciprocal lattice can be calculated from the CBED pattern as

$$H = K - K \sqrt{1 - (R/L)^2}$$

where K is the reciprocal of the incident electron wavelength, R is the radius of a high order Laue ring, and L is the camera length.

By using the above equation, the γ -Fe₂O₃ unit cell is consistently derived from all three primary zone axis patterns to be cubic with lattice parameter approximately equal to three times that of the magnetite crystal lattice parameter. Fig. 10 is a series of CBED $\langle 110 \rangle$ patterns taken from the same area of a particle during prolonged exposure. Under the convergent electron beam, the ordered structure with lattice parameter 25Å is observed to gradually change to a disordered structure with lattice parameter 8.33Å. This result suggests disordering has occurred so that vacancies are no longer uniformly distributed in each unit cell. Fig. 11 shows similar order-disorder transitions observed in a crystal having $\langle 100 \rangle$ zone axis. This transition has also been observed in crystals having $\langle 111 \rangle$ zone axis. The resultant disordered structure continues to have the $m\bar{3}m$ point group symmetry, as shown in Fig. 12.

(B) Microstructural Studies

Table 5 contains a summary of previous microstructural studies²²⁻²⁷ on the $\gamma\text{-Fe}_2\text{O}_3$. It is evident that there exist many discrepancies. However, it should be borne in mind that $\gamma\text{-Fe}_2\text{O}_3$ can be prepared by several methods which might lead to different results.

In this part of the study, the main interest was to examine the microstructural features, namely the crystalline nature and the long axis directions of the particles, in commercial particles used today. Since even the smallest intermediate aperture (0.5 μm) is relatively large, it almost always covers more than one particle. Hence, the simple SAD experiments is not suitable. Using other methods described in section III(B), in Fig. 13 micrograph b was obtained from spot A and similar patterns as in micrograph c were obtained from spots B, C and D. It can be seen that the long axis of the particle is along $\langle 111 \rangle$. Also, since the orientation of these patterns has not changed, it is clear that the particle is a single crystal. In Fig. 14, using the same method, the particle in micrograph a is a single crystal but now the axis is observed to be $\langle 100 \rangle$. Similarly, in Fig. 15, the particle in a tape sample also shows the single crystal nature but with the long axis along $\langle 110 \rangle$. This single crystal nature of the particles is also confirmed by dark-field imaging, in which an entire particle is in bright contrast, as shown in Fig. 16.

In about 40 observations such as these and those using microdiffraction technique as shown in Fig. 17, it was found that about 30% of the particles had the long axis along $\langle 110 \rangle$ and 40% with their long axes inclined less than 30° to $\langle 110 \rangle$.

(C) Non-magnetic Properties

Besides magnetic properties, several non-magnetic properties also play important roles in determining the performance. In SEM observations on commercial tapes, conclusions may be drawn as to the morphology and tape performance by reference to Fig. 1. For example:

(1) Improve particle alignment

In all tape samples, particles are aligned along the longitudinal direction of the tape so as to improve the coercivity. But between tapes (SA and D tapes are supposed to give the best and worst performance among the three, respectively.) it was obvious that SA tapes have the best alignment and D tape has the poorest.

(2) Reduce particle size

Small particle size can reduce modulation noise and surface roughness and thereby increase signal to noise ratio. AD tape apparently has a smaller particle size than D tape. Since SA tape is made of cobalt-absorbed particles, it can not be compared with other two tapes.

(3) Higher packing density

Higher packing density means a higher amount of particles switched by the signal, thereby producing higher output. Qualitatively, it can be seen from the micrograph that SA tapes have the highest packing density, followed by the AD tape and D tape.

V. Discussion

The CBED results have revealed that γ -Fe₂O₃ has a cubic superstructure unit cell of lattice parameter approximately three times that of the magnetite lattice parameter. Thus, each unit cell is converted from 27 magnetite unit cells, with $8/3 \times 27 = 72$ iron vacancies distributed in ordered configuration in the superstructure unit cell.

The observed transition from ordered structure to disordered structure suggests iron vacancy disordering has occurred under the electron beam. The resultant cubic unit cell with lattice parameter approximately equal to that of magnetite indicates that iron vacancies are no longer evenly distributed in each unit cell. This local uneven iron vacancy distribution will induce local fluctuation in magnetization which may in turn be the cause of noise. Therefore, the disordered structure is undesirable.

The origin of the order-disorder transition has been examined. The same pattern as Fig. 11(f) is obtained after re-examining the same area also in a liquid nitrogen cold stage several days later. This result confirms that the order-disorder transition is not due to local specimen heating by the electron beam. Furthermore, at 100 kV, knock-on displacement damage is not likely to take place in an ionic material³³. However, electrons may transfer,

by ionization damage, sufficient momentum to enhance cation diffusion, especially in a high defect density material such as $\gamma\text{-Fe}_2\text{O}_3$. In such cases the activation energy required for cation diffusion is low so that diffusion may be enhanced by electrons of energy even less than 100 keV³³. Thus, the mechanism of this order-disorder transition is considered to be due to radiation-enhanced diffusion of cations in the electron beam. No attempt has been made in this work to measure this quantitatively.

The result of microstructural study showed that $\gamma\text{-Fe}_2\text{O}_3$ particles were single crystals which proved that previous interpretations of the low coercivity value, in terms of polycrystalline particles, cannot be correct. An alternative condition that satisfies the fanning chain-of-sphere reversal mode may be responsible for the low coercivity value. That is these particles may consist of several single domain regions and the domain walls are somewhat pinned (by the holes, for example).

In order to examine this, domain wall observations using Lorentz microscopy techniques^{34,35} have been tried on the Philips EM 301. However, because of the small particle size and the magnification limitation, because the objective lens must be turned off, the experiment was not successful.

Domain wall observation on these tiny particles requires a modified electron microscope which can provide high magnification while the specimen area has a low magnetic field. Such facilities were not available for this research.

The long axis directions of the particles were found to be along low order crystallographic directions which indicates that crystal anisotropy was not fully exploited. The coercivity of the particles may be increased by having the long axes along $\langle 110 \rangle$ directions. From topotactic transformation arguments²⁶ (i.e. the transformation of one solid crystalline phase to another by rearrangement of the atoms so that even if a certain fraction of the material is taken into or expelled from the system the phases have a definite crystallographic structure relationship to each other), the long axis direction seems could be deduced from the starting material, as shown in Table 6.

Several important aspects of this material require further experiments:

- (1) Environmental effects on the structure. Since $\gamma\text{-Fe}_2\text{O}_3$ has a high defect density, the cation diffusion may also be enhanced by thermal energy. The extent of thermal effects can be revealed by heating experiments at temperatures below the transition temperature of $\gamma\text{-Fe}_2\text{O}_3$ to $\alpha\text{-Fe}_2\text{O}_3$.

(2) Domain wall observations. Lorentz electron microscopy experiments can help in understanding the origin of the coercivity and the magnetization reversal mechanism which may in turn provide the information needed for further improvement of the material.

(3) To establish the factor(s) that affect the morphology controlling the long axis directions of the particle. Since the crystal anisotropy accounts for 1/3 of the room temperature coercivity, crystals having their long axes along $\langle 110 \rangle$ directions can increase the coercivity by a certain amount.

VI. Conclusion

Because of the difficulties in obtaining information directly from individual particles, there are many discrepancies in the literature regarding the structure and microstructure of $\gamma\text{-Fe}_2\text{O}_3$ particles. In this study, whereby individual particles have been examined by electron microscopy and microdiffraction, the following conclusions have been made:

(1) $\gamma\text{-Fe}_2\text{O}_3$ particles prepared for commercial audio tapes have a primitive cubic lattice and $m\bar{3}m$ point group, therefore the space group of the material can only be one of four possible space groups.

(2) The material has a cubic superstructure with a threefold increase in lattice parameter as a result of cation vacancy ordering.

(3) An order-disorder transition occurs by electron irradiation during observation. This transition is probably due to enhanced diffusion by ionization damage.

(4) Morphological studies showed that these particles are single crystals; thereby denying concepts that such iron oxide particles are polycrystalline. The origin of the coercivity requires further examination.

(5) The long axis directions of the particles are found to be along low order crystallographic directions with about 30% along $\langle 110 \rangle$.

Acknowledgements

I would like to express my deepest appreciataion to Professor Gareth Thomas for his encouragement, guidance and support throughout this work. Dr. Edward Goo's interest in this work and helpful discussions are also gratefully acknowledged. Thanks are also extended to the TDK company of Japan and Hercules Incorporated for supplying the γ -Fe₂O₃ particles used in this study.

This work was supported by the Director, Office of Energy Research, Office of Basic Energy Sciences, Division of Materials Sciences of the U. S. Department of Energy under contract No. DE-AC03-76SF00098.

References

1. M. Camras, US patent 2 694 656 (1954)
2. L. M. Bennetch, H. S. Greiner, K. R. Hancock and M. Hoffman, US patent 3 904 540 (1975)
3. L. H. Van Vlack, Elements of Materials Science and Engineering, Ch. 8, pp. 307 (1980)
4. B. D. Cullity, Introduction to Magnetic Materials, Ch. 6, pp. 201 (1972)
5. G. Bate, Ferromagnetic Materials, Vol. 2, Ed. E. P. Wohlfarth, Ch. 7, pp. 443 (1980)
6. H. Takei and S. Chiba, J. Phys. Soc. Japan, 21, 1255 (1966)
7. D. F. Eagle and J. C. Mallinson, J. Appl. Phys., 38, 995 (1967)
8. B. D. Cullity, Introduction to Magnetic Materials, Ch. 7, pp. 243 (1972)
9. G. Bate and J. K. Alstad, IEEE, Mag-5, 821 (1969)
10. I. S. Jacobs and C. P. Bean, Phys. Rev., 100, 1060 (1955)
11. E. H. Frei, S. Shtrikman and D. Treves, Phys. Rev., 106, 446 (1957)
12. G. Z. Hägg, Phys. Chem. 29B, 95 (1935)
13. E. J. W. Verwey, Z. Krist, 91, 65 (1935)
14. L. Néel, Ann. Phys., 3, 137 (1948)
15. G. R. Ferguson and M. Hass, Phys. Rev. 112, 1130 (1958)

16. G. W. Van Oosterhout and C. J. M. Rooijmans, *Nature* **181**, 44 (1958)
17. P. B. Braun, *Nature*, **170**, 1123 (1952)
18. R. Haul and T. Schoon, *Z. Phys. Chem.*, **B44**, 216 (1939)
19. M. G. Chaudron, *CR Acad. Sci.*, **214**, 619 (1957)
20. R. Ueda and K. Hasegawa, *J. Phys. Soc. Japan*, **17**
Suppl. BII, 391 (1962)
21. M. Boudeulle, H. Batis-Landoulsi, Ch. Leclercq and
P. Vergnon, *J. solid state Chem.*, **48**, 21 (1983)
22. W. P. Osmond, *Proc. Phys. Soc. (London)*, **66**, sec.B,
265 (1953)
23. R. B. Campbell, *J. Appl. Phys.*, **28**, 381 (1957)
24. J. Hurt, A. Amendola and R. E. Smith, *J. Appl. Phys.*,
37, 1170 (1966)
25. B. Gustard and H. Vriend, *IEEE Trans. Magn.*, **Mag-5**, 327
26. G. W. Van Oosterhout, *Acta Cryst.*, **13**, 932 (1960)
27. G. Bate, *Ferromagnetic Materials*, Vol. 2,
Ed. E. P. Wohlfarth, *Ch. 7*, pp. 381 (1982)
28. Audio tapes were provided by the TDK company, 1-13-1
Nihonbashi Chyuohku, Tokyo, Japan, and powder particles
were provided by Hercules Incorporated, Wilmington,
DE 19899, U.S.A.
29. J. W. Steeds, *Introduction to Analytical Electron*
Microscopy, Ed. J. J. Hren, J. I. Goldstein and
D. C. Joy, *Ch. 15*, pp. 387 (1979)

30. B. F. Buxton, J. A. Eades, J. W. Steeds and G. M. Rackham
Phil. Trans. R. Soc. 281, 171 (1976)
31. J. W. Steeds, G. M. Rackham and M. D. Shannon, Inst.
Phys. Conf. Ser. No. 41, Chap. 3, 135 (1978)
32. D. B. Williams, Practical Analytical Electron Micro-
scopy in Materials Science, Ch. 6, 117 (1984)
33. L. W. Hobbs, Introduction to Analytical Electron
Microscopy, Ed. J. J. Hren, J. I. Goldstein and
D. C. Joy, Ch. 17, 437 (1979)
34. G. Thomas and M. J. Goringe, Transmission Electron
Microscopy of Materials, Ch. 3, pp. 185 (1979)
35. P. Hirsch, A. Howie, R. B. Nicholson, D. W. Pashley,
and M. J. Whelan, Electron Microscopy of Thin Crystals,
Ch. 16, pp. 388 (1977)

Figure captions

- Figure 1. SEM images of commercial magnetic tapes. (a) D tape (b) AD tape and (c) SA tape, showing different particle alignment, packing density and particle size.
- Figure 2. Spinel structure. The magnetic moment of these cations in octahedral sites (CN=6) and those in tetrahedral sites (CN=4) have opposing alignments. (After Van Vlack [3].)
- Figure 3. CBED $\langle 111 \rangle$ zone axis pattern of $\gamma\text{-Fe}_2\text{O}_3$ particle showing a $3m$ symmetry.
- Figure 4. X-ray diffraction traces of $\gamma\text{-Fe}_2\text{O}_3$ showing several non-magnetic extra lines.
- Figure 5. Microdiffraction patterns of $\gamma\text{-Fe}_2\text{O}_3$ from (a) $\langle 100 \rangle$ and (b) $\langle 110 \rangle$ zone axis. Forbidden reflections for the fcc structure such as 100, 110, 210 etc. are allowed indicating the lattice is a primitive cubic.
- Figure 6. CBED zone axis patterns from tape samples showing a cubic threefold superstructure. (a) $\langle 100 \rangle$, (b) $\langle 110 \rangle$ and (c) $\langle 111 \rangle$ pattern.
- Figure 7. CBED zone axis patterns from powder samples also showing a cubic threefold superstructure. (a) $\langle 100 \rangle$, (b) $\langle 110 \rangle$ and (c) $\langle 111 \rangle$ pattern.
- Figure 8. CBED patterns showing $m3m$ point group symmetry. (a) $\langle 100 \rangle$, (b) $\langle 110 \rangle$ and (c) $\langle 111 \rangle$ pattern.

Figure 9. Schematic illustration of electron diffraction illustrating the formation of higher order Laue zones.

Figure 10. $\langle 110 \rangle$ CBED patterns showing a transition from an ordered structure (a) to a disordered structure (f). The time lapse (a)-(f) is approximately 40 minutes.

Figure 11. $\langle 100 \rangle$ CBED patterns showing a transition from an ordered structure (a) to a disordered structure (f). The time lapse (a)-(f) is approximately 25 minutes.

Figure 12. Zone axis patterns of disordered structure showing the structure continues to have the $m3m$ point group, following structure disordering.

Figure 13. (a) Bright field image, (b) and (c) are $\langle 110 \rangle$ patterns from A, B, C and D spots in (a) showing the particle is a single crystal and the long axis is along $\langle 111 \rangle$ directions.

Figure 14. (a) Bright field image, (b), (c) and (d) are $\langle 100 \rangle$ patterns from different areas along the particle showing it is a single crystal and the long axis is along $\langle 100 \rangle$ directions.

Figure 15. (a) Bright field image, (b) and (c) are $\langle 110 \rangle$ patterns from spots A and B, respectively. The particle is a single crystal and the long axis is along $\langle 110 \rangle$ directions.

Figure 16. (a) Bright field image, (b) corresponding dark field image showing the particle is a single crystal.

Figure 17. (a) Bright field image, (b) $\langle 111 \rangle$ pattern and (c) $\langle 112 \rangle$ pattern showing the long axis is along $\langle 110 \rangle$ directions.

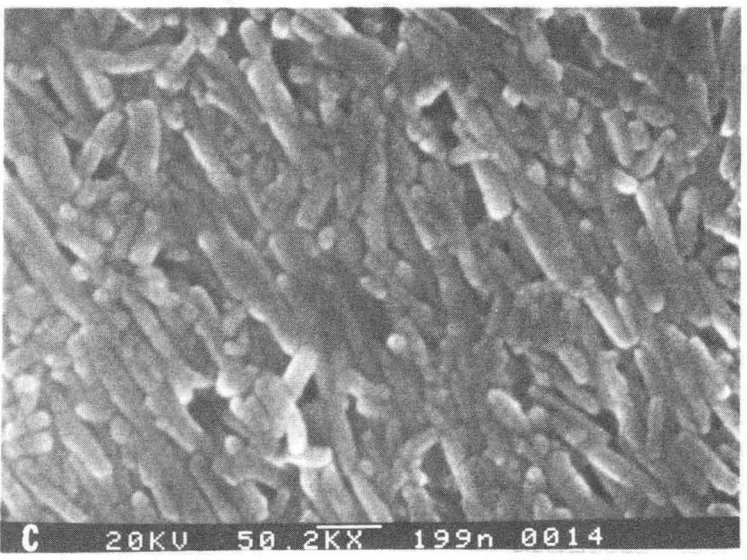
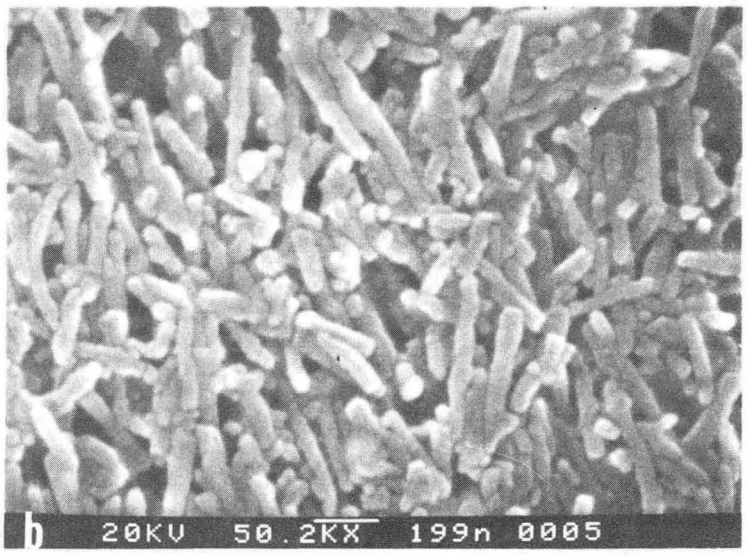
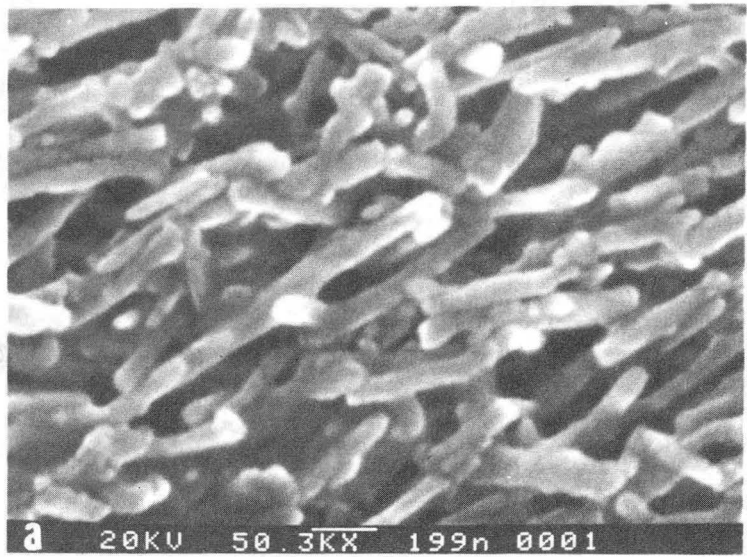


Fig. 1

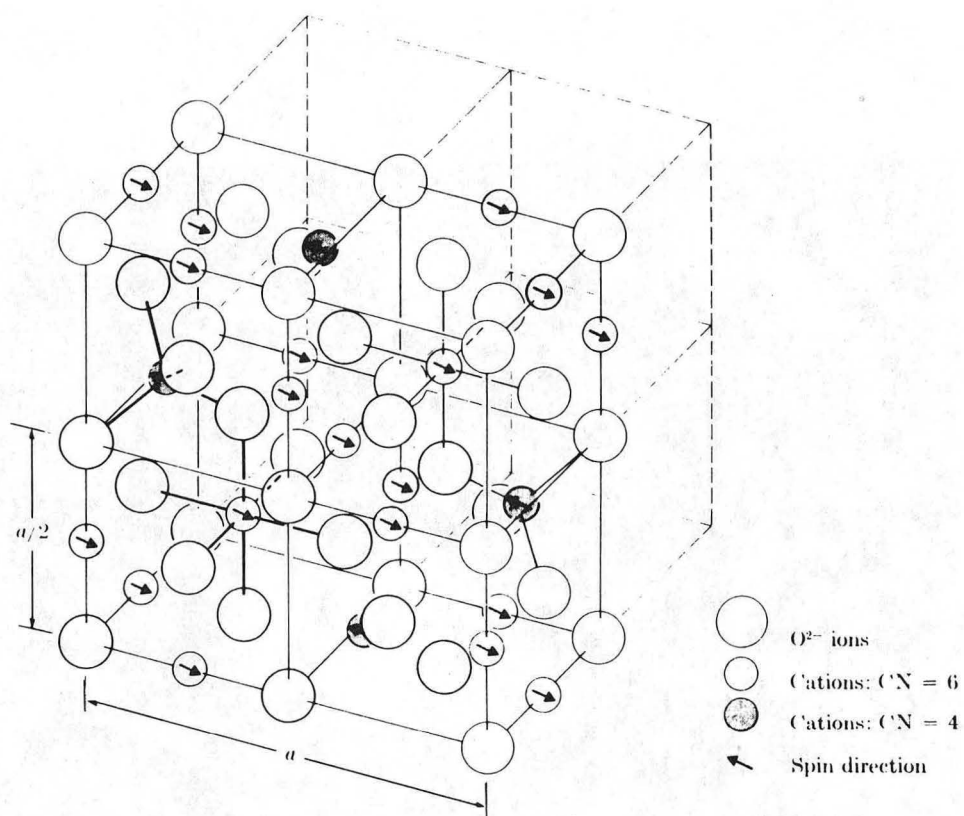


Fig. 2

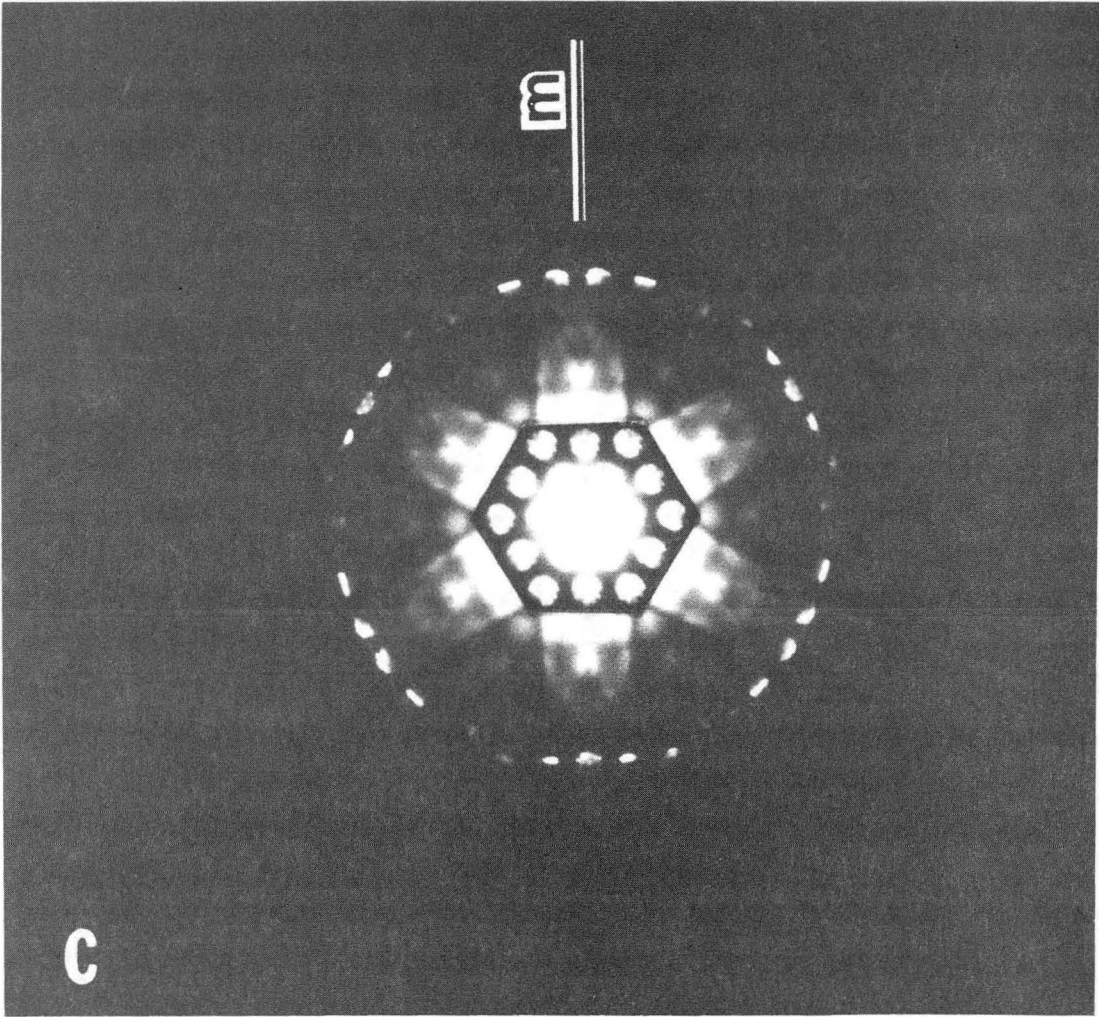


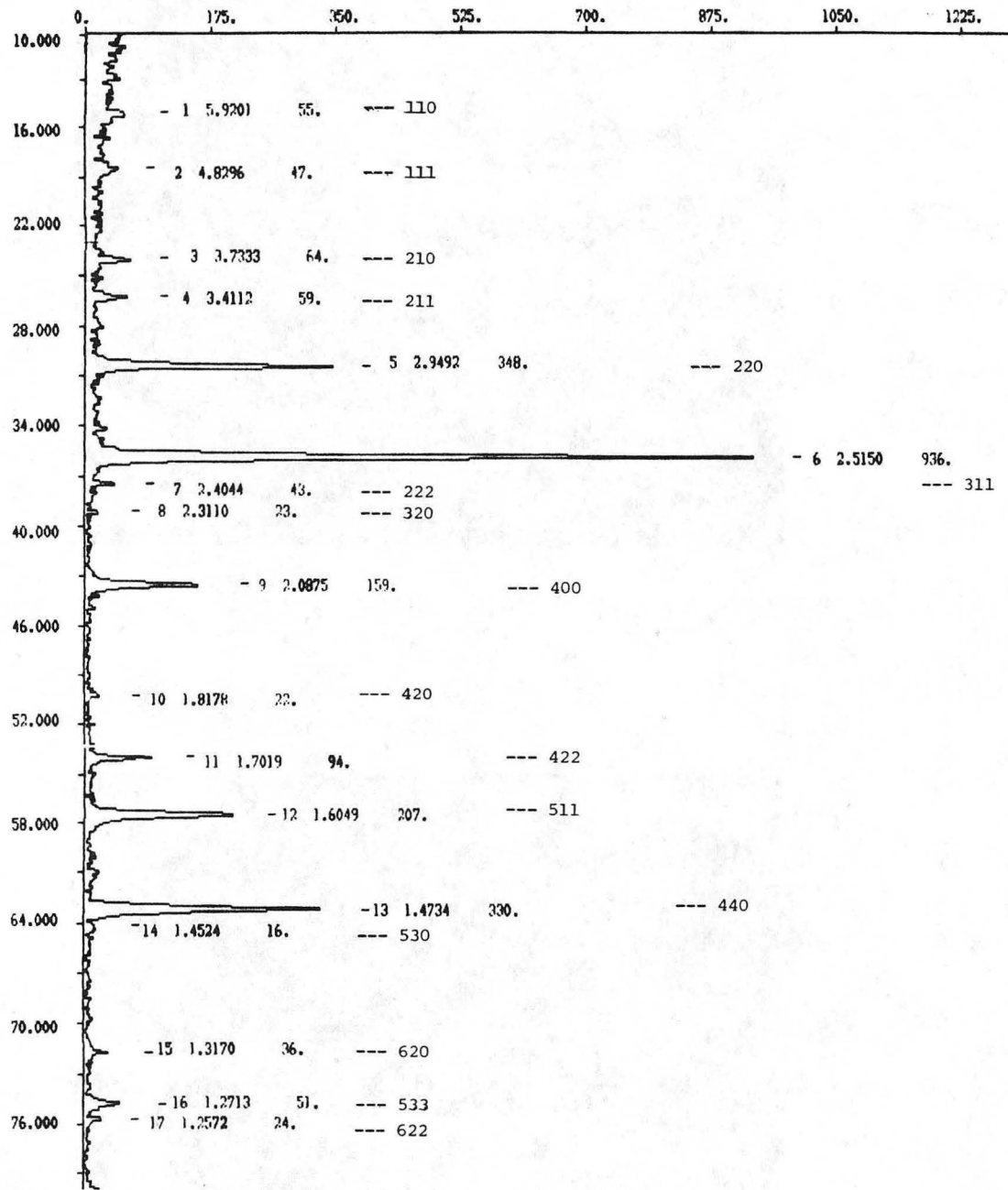
Fig. 3

XBB 854-2973

SLITS 1 1 1 .05 .05,
T 1.000, S 0.100 [99]

Anode : CU, Lambda : 1.5405

FE2O3



CMD>

Fig. 4

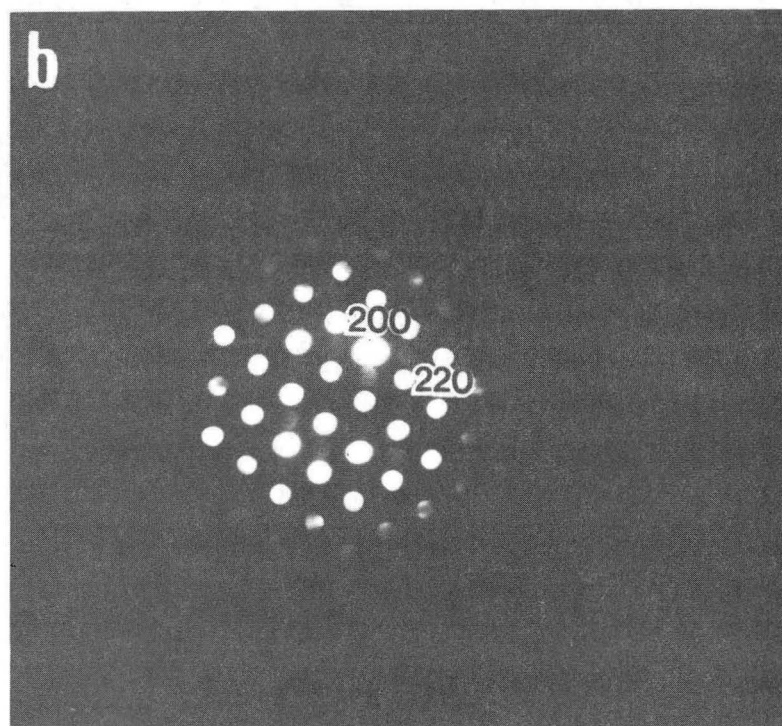
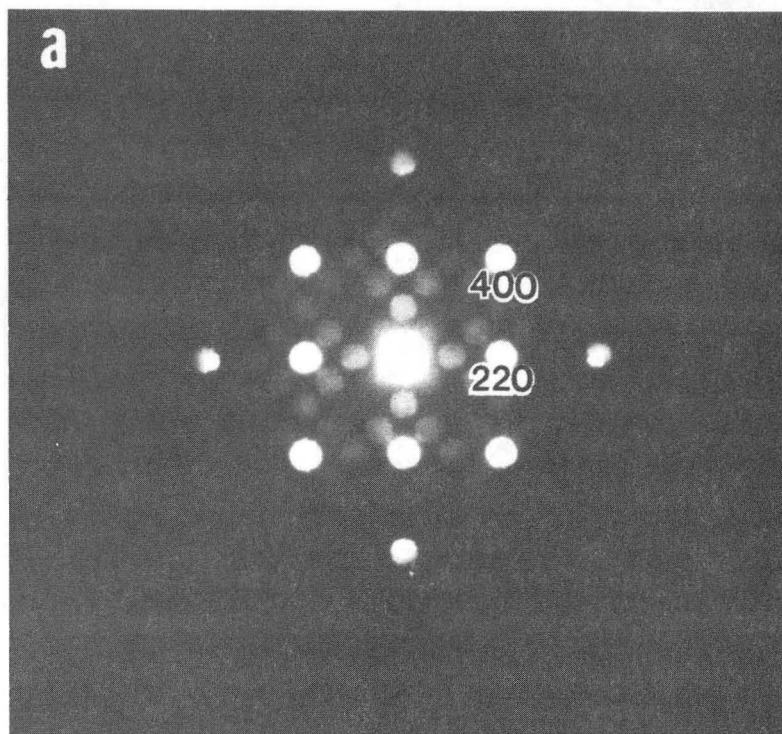


Fig. 5

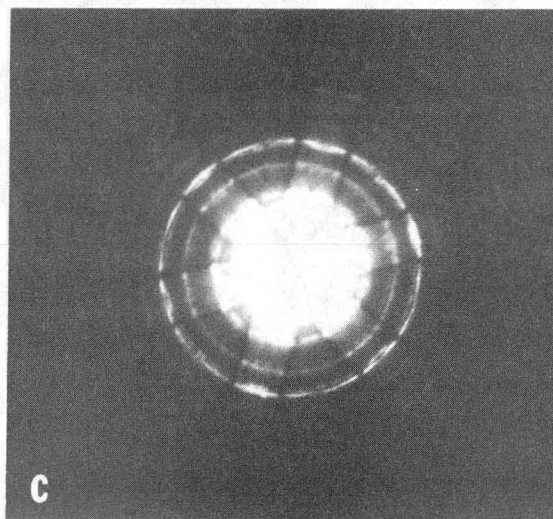
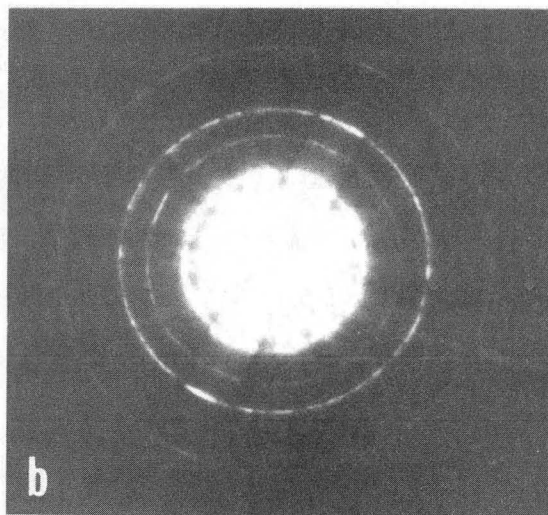
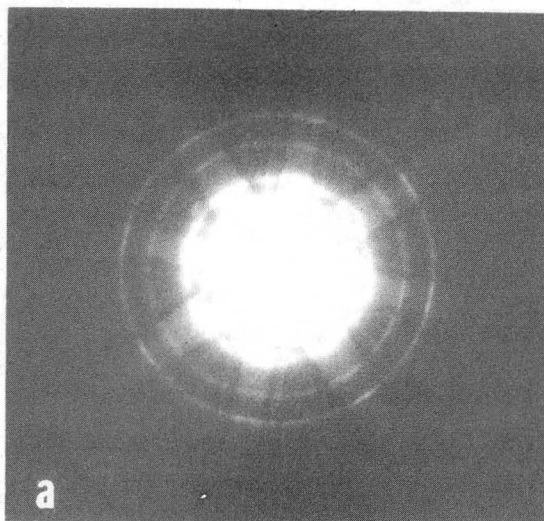


Fig. 6

XBB 854-2970

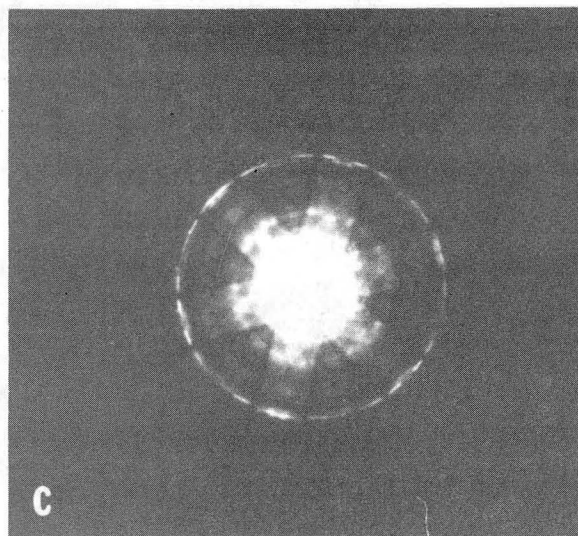
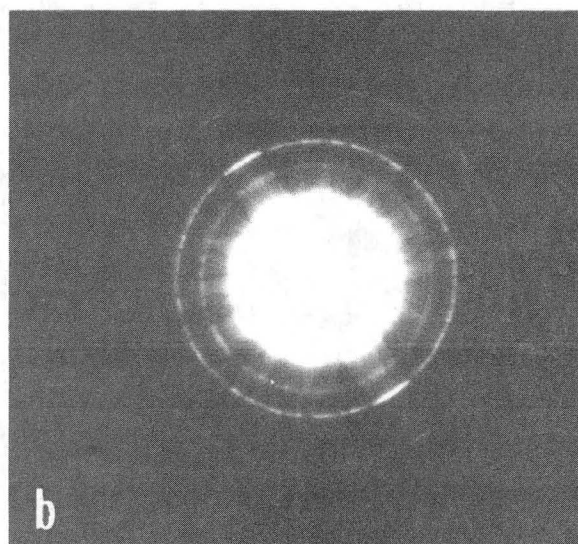
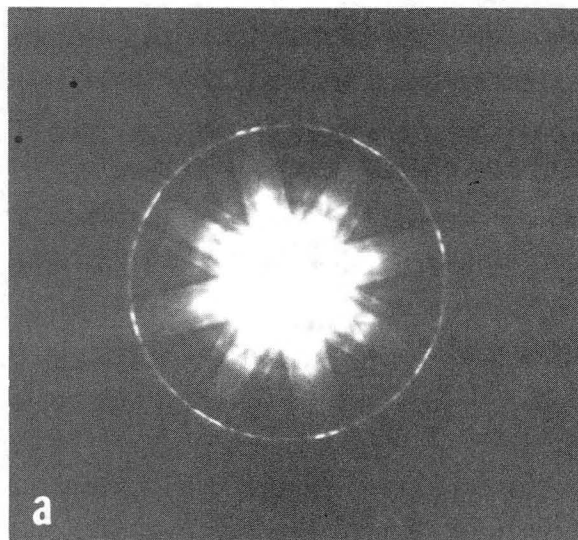


Fig. 7

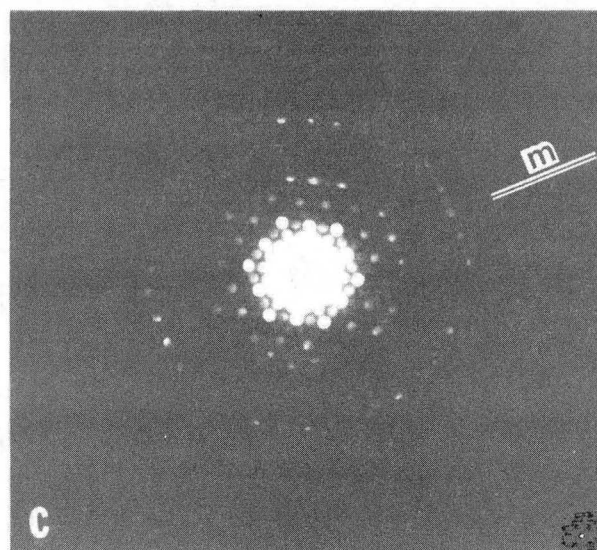
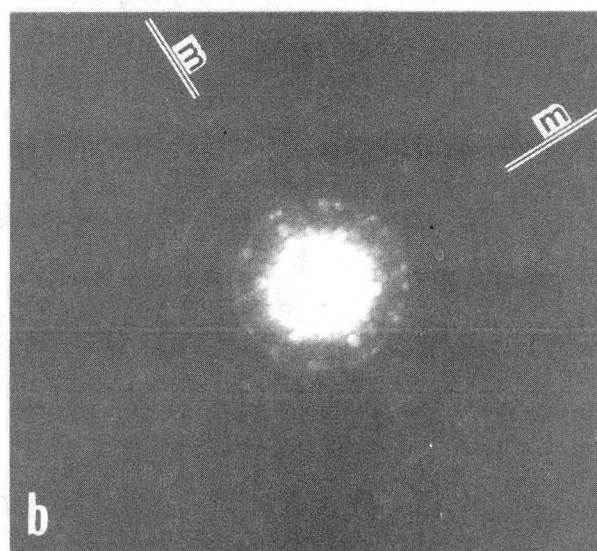
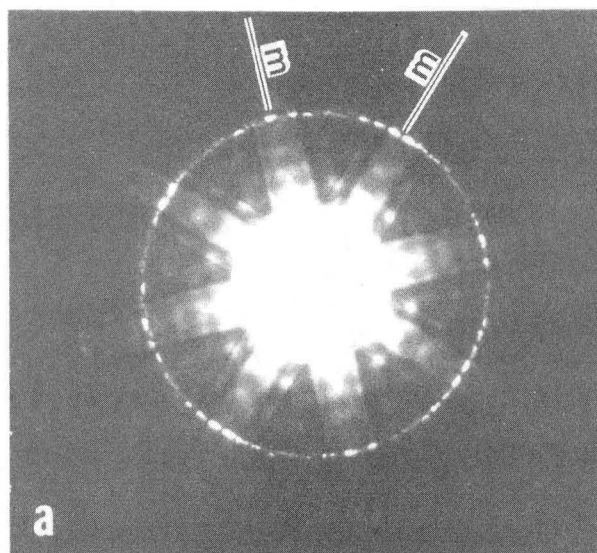
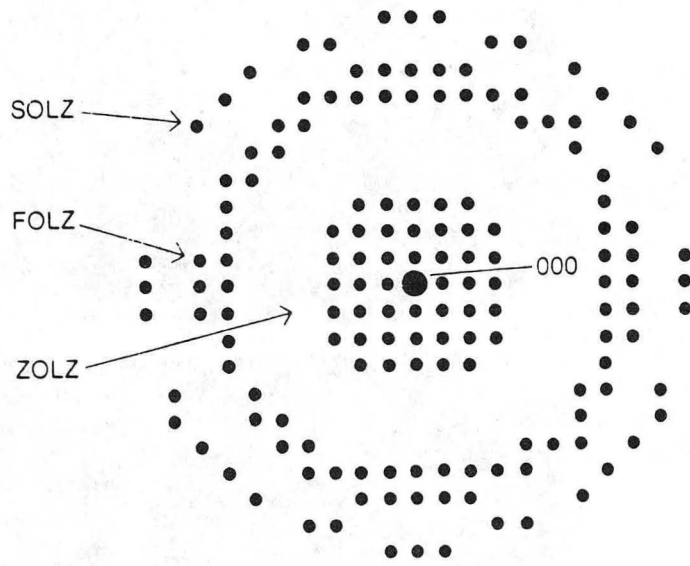
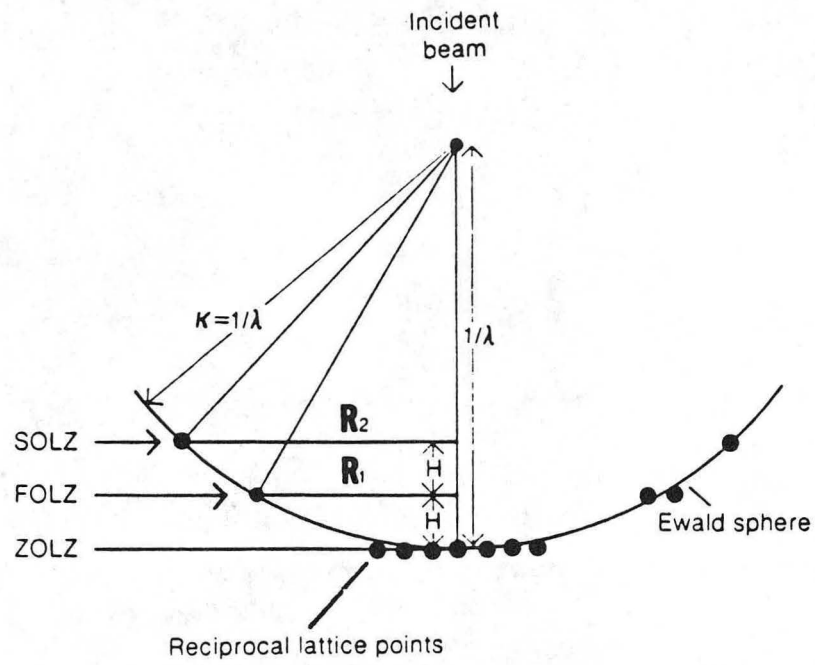


Fig. 8



$$H = K - K \sqrt{1 - (R/L)^2}$$

XBL 858-3751

Fig. 9

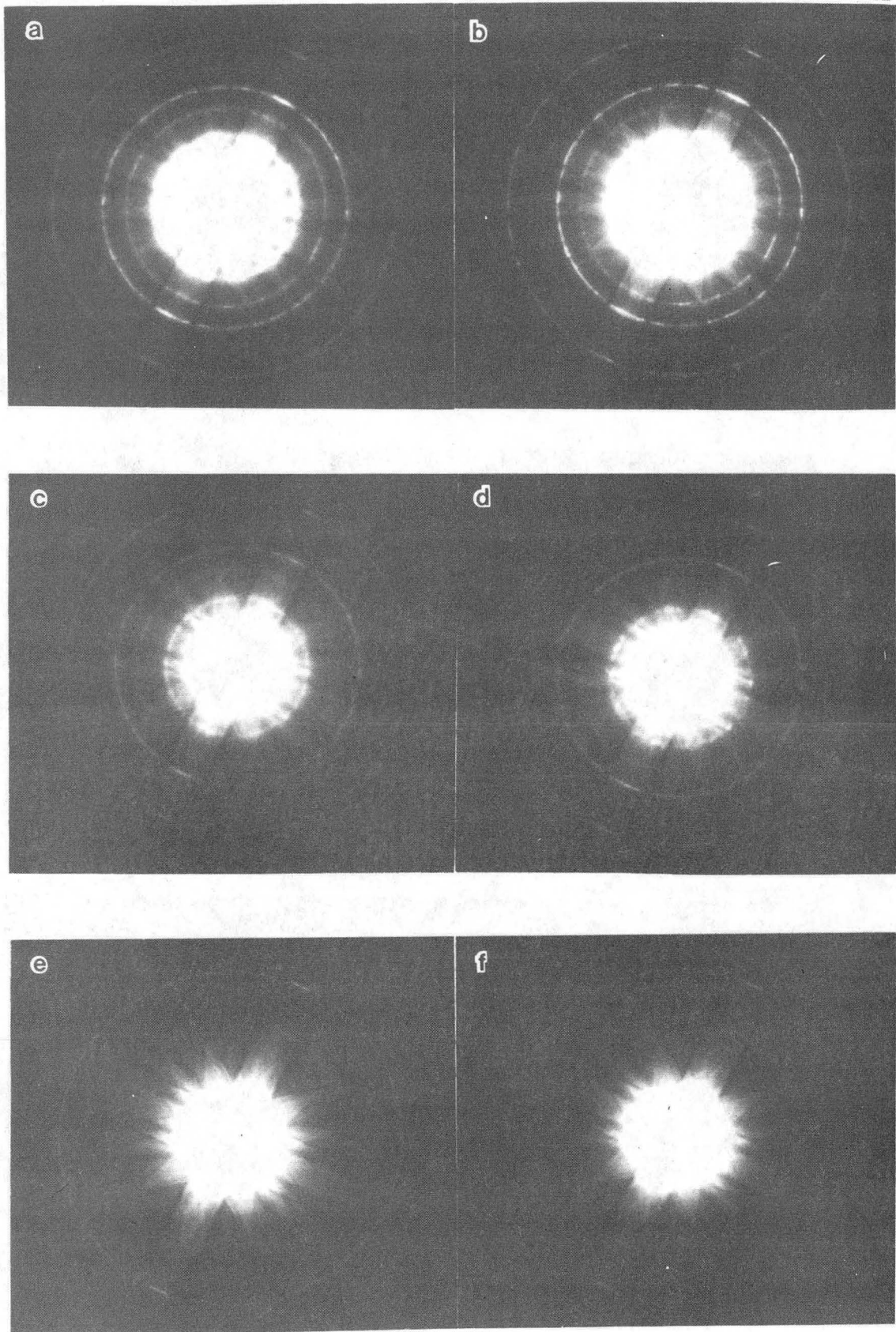


Fig. 10

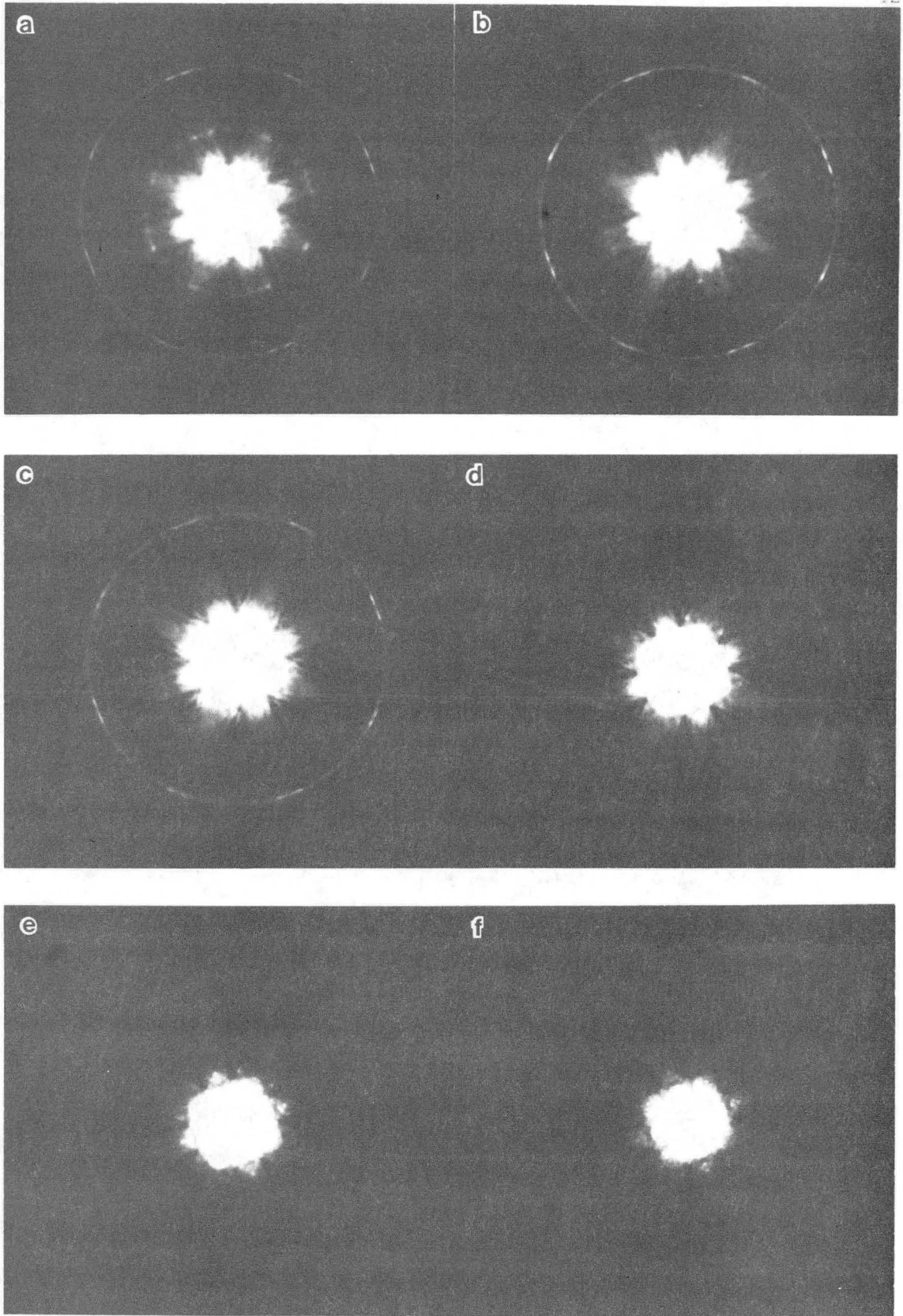


Fig. 11.

XBB 857-5721

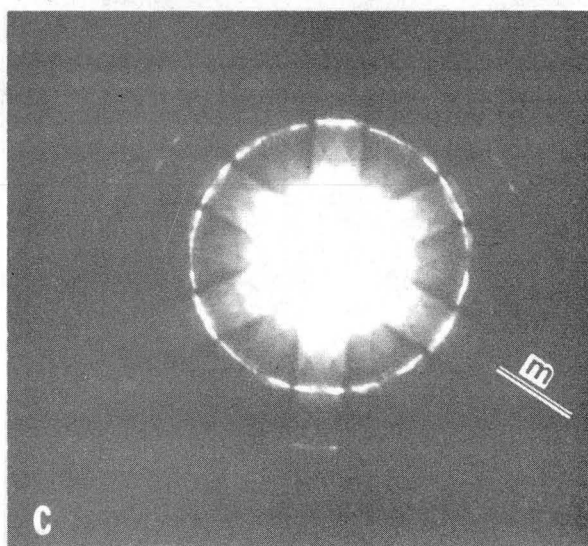
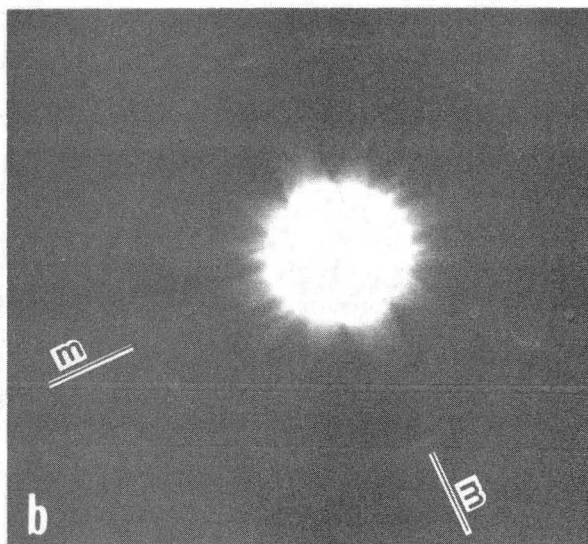
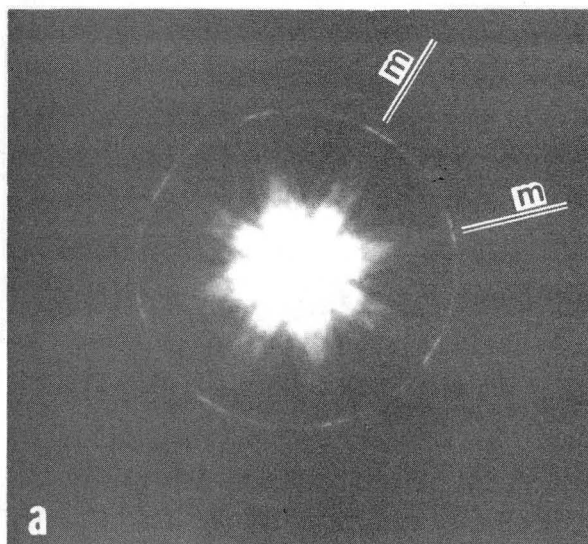


Fig. 12

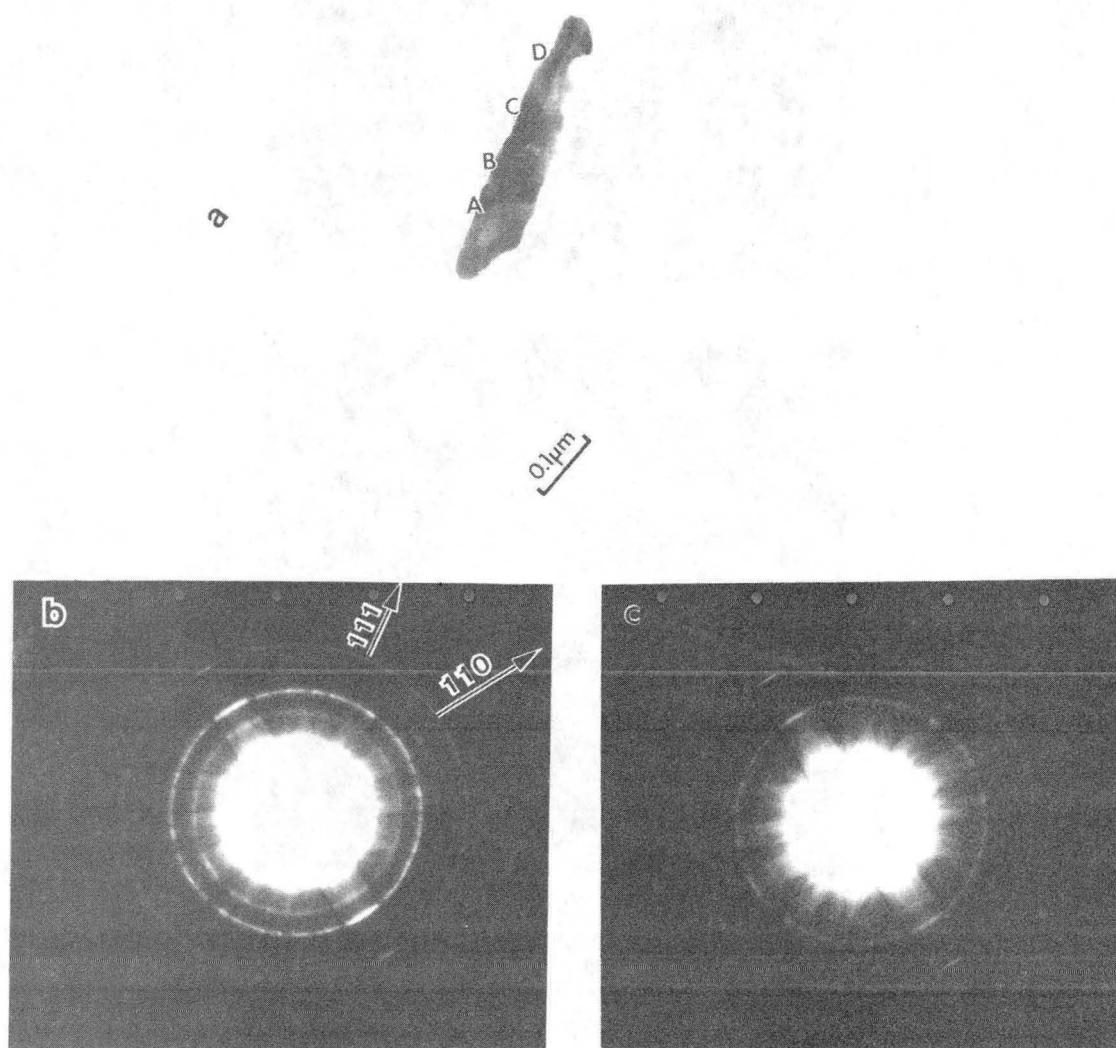


Fig. 13

XBB 354-2967

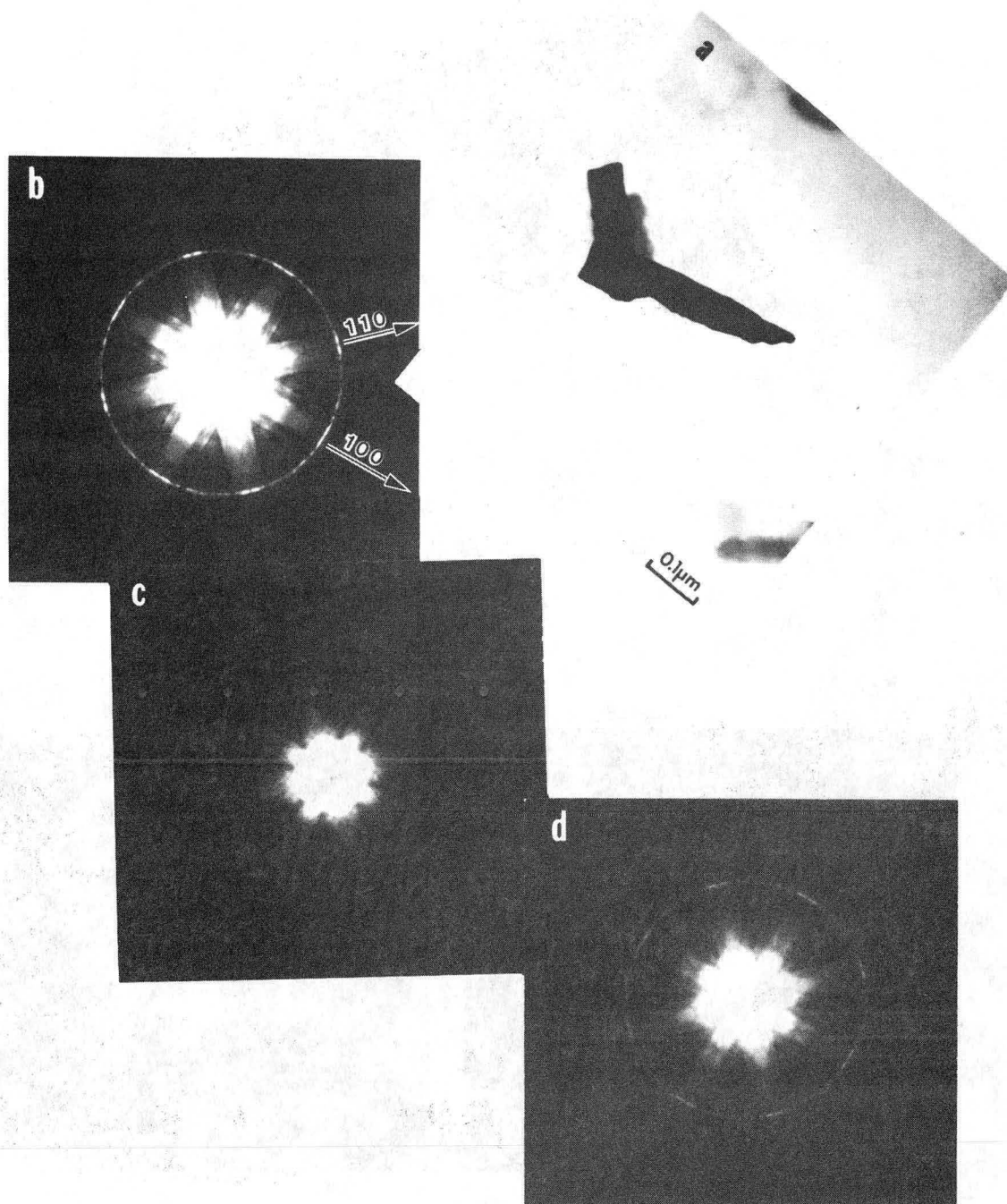


Fig. 14

XBB 854-2966

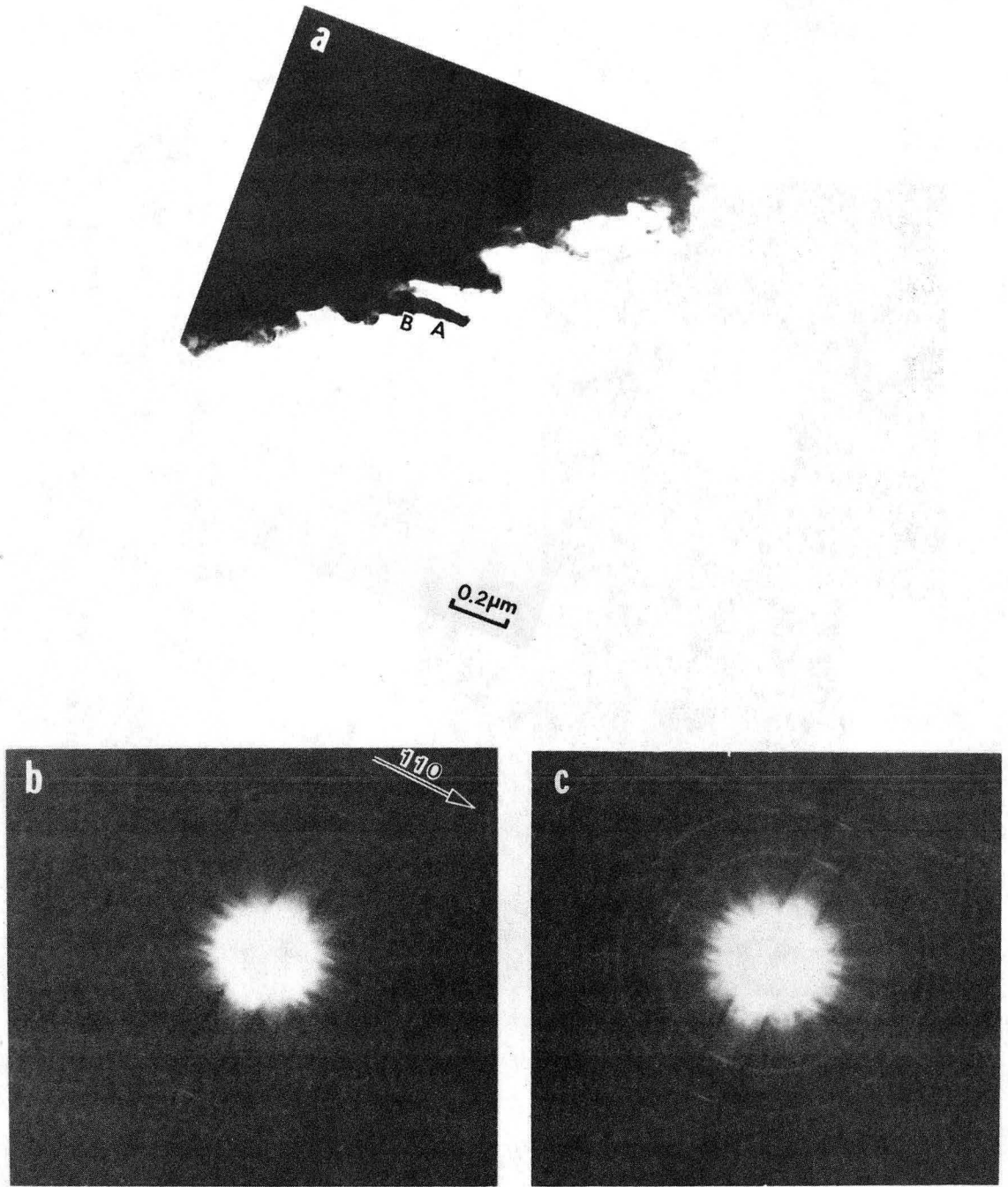


Fig. 15

XBB 854-2961

a



0.2 μ m

b

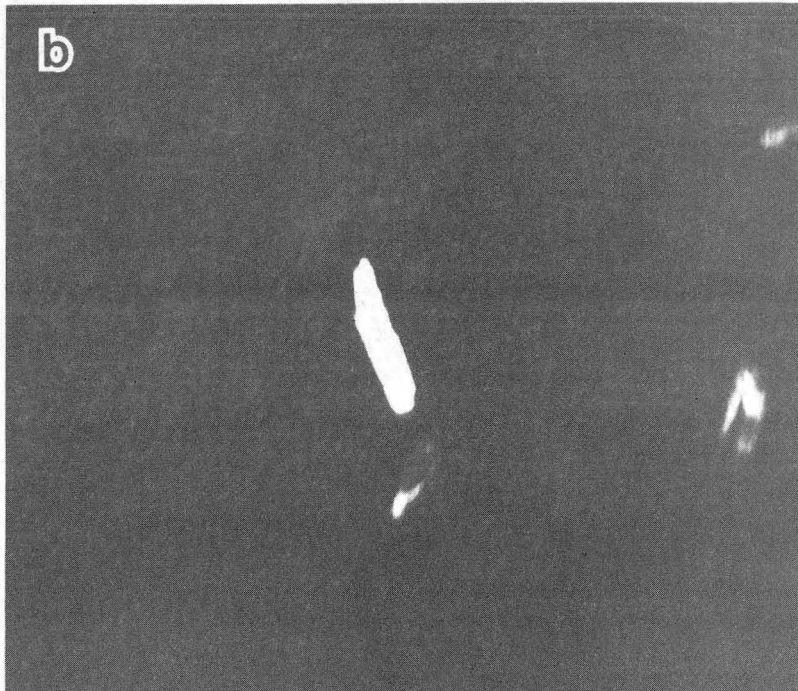


Fig. 16

XBB 854-2964

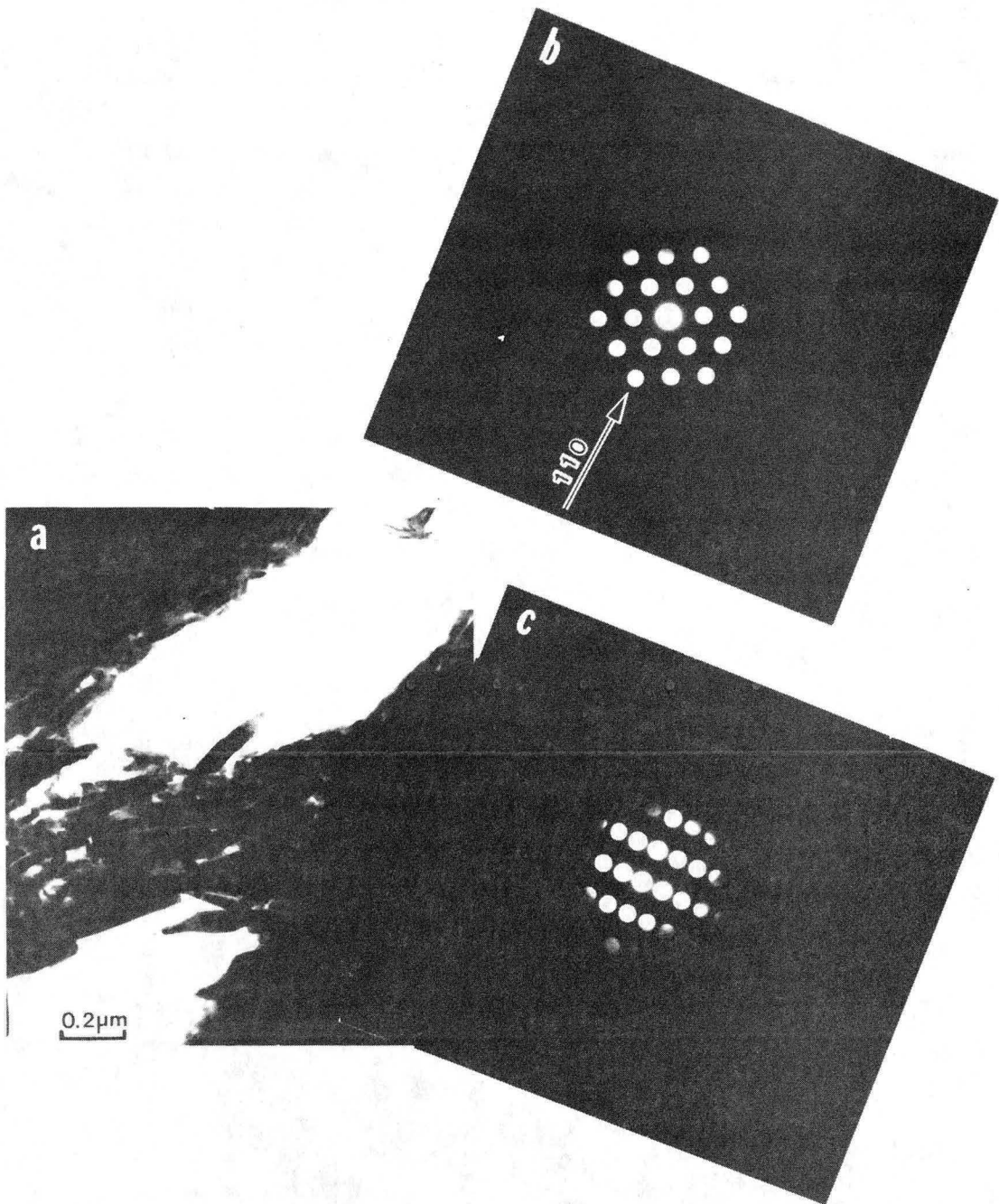
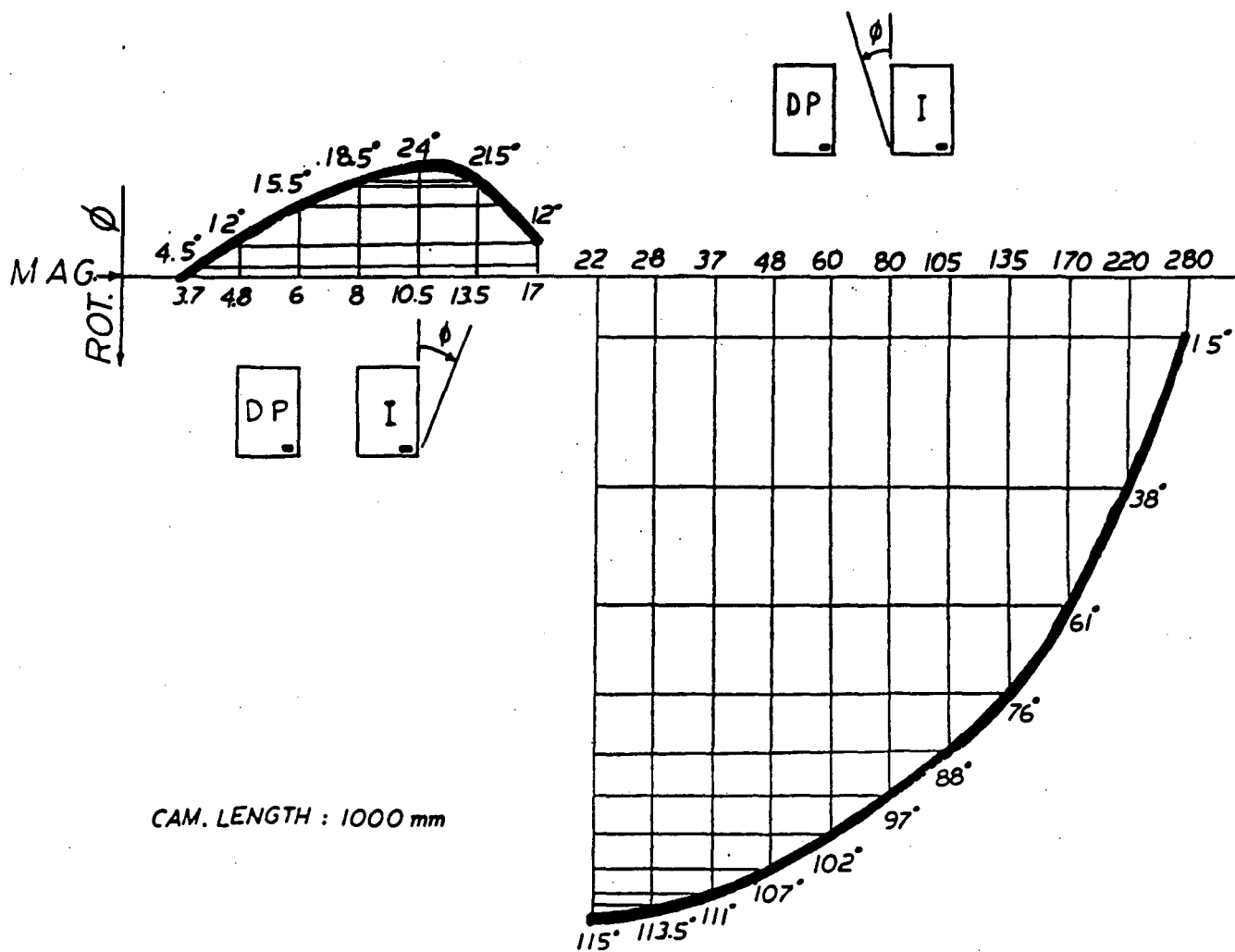


Fig. 17

XBB 854-2965

Table. 1 Philips EM400 TEM/STEM Analytical Microscope Rotation Calibration



To use the above graph for camera lengths other than 1000 mm, simply add the required number of counter-clockwise degrees as read from the table below to the rotation angle read from the graph.

Camera Length	Additional Counter-clockwise Angle
120	97.1
200	120.2
280	142.9
450	4.3
600	3.8
750	1.1
1000	-
1400	1.0
1800	3.0
2400	6.3
3300	12.1

Table 2. Published structural studies on $\gamma\text{-Fe}_2\text{O}_3$

<u>Author</u>	<u>Technique</u>	<u>Vacancy Distribution</u>	<u>Space Group</u>
Hagg ¹²	X-ray diffraction	distribute uniformly in the cation sites	Fd3m
Verwey ¹³	same as above	same as above	
Neel ¹⁴	saturation magnetization measurement	only over the octahedral sites	
Ferguson and Hass ¹⁵	neutron diffraction	only in the octahedral sites	
Haul and Schoon ¹⁶	X-ray diffraction	vacancy ordering result in a primitive lattice	
Chaudron ¹⁷	same as above	same as above	
Braun ¹⁸	same as above	same as above	$P4_1$ with $c/a=3$
Van Oosterhout and Rooijmans ¹⁹	same as above	same as above	$P4_1$ 32
Ueda and Hasegawa ²⁰	X-ray and neutron diffraction	occupy only four of the 16d sites	
Takei ⁶ and Chiba	X-ray diffraction	no vacancy ordering	
Beudelle et. al. ²¹	X-ray and electron diffraction	either with noncubic symmetry or with cubic superstructure with a threefold unit cell	

Table 3. CBD Pattern Symmetries*
 (Where a Dash Appears in Column 7, the Special Symmetries Can Be Deduced from Columns 5 and 6 of This Table (or from Table 1 in Buxton et al 1976).)

Diffraction Group	Bright Field	Whole Pattern	Dark Field		$\pm G$		Projection Diffraction Group
			General	Special	General	Special	
1	1	1	1	none	1	none	1 _R
1 _R	2	1	2	none	1	none	
2	2	2	1	none	2	none	21 _R
2 _R	1	1	1	none	2 _R	none	
21 _R	2	2	2	none	21 _R	none	
m _R	m	1	1	m	1	m _R	m1 _R
m	m	m	1	m	1	m	
m1 _R	2mm	m	2	2mm	1	m1 _R	
2m _R m _R	2mm	2	1	m	2	—	2mm1 _R
2mm	2mm	2mm	1	m	2	—	
2 _R mm _R	m	m	1	m	2 _R	—	
2mm1 _R	2mm	2mm	2	2mm	21 _R	—	
4	4	4	1	none	2	none	41 _R
4 _R	4	2	1	none	2	none	
41 _R	4	4	2	none	21 _R	none	
4m _R m _R	4mm	4	1	m	2	—	4mm1 _R
4mm	4mm	4mm	1	m	2	—	
4 _R mm _R	4mm	2mm	1	m	2	—	
4mm1 _R	4mm	4mm	2	2mm	21 _R	—	
3	3	3	1	none	1	none	31 _R
31 _R	6	3	2	none	1	none	
3m _R	3m	3	1	m	1	m _R	3m1 _R
3m	3m	3m	1	m	1	m	
3m1 _R	6mm	3m	2	2mm	1	m1 _R	
6	6	6		none	2	none	61 _R
6 _R	3	3		none	2 _R	none	
61 _R	6	6	2	none	21 _R	none	
6m _R m _R	6mm	6	1	m	2	—	6mm1 _R
6mm	6mm	6mm	1	m	2	—	
6 _R mm _R	3m	3m	1	m	2 _R	—	
6mm1 _R	6mm	6mm	2	2mm	21 _R	—	

*After Buxton et al 1976.

Table 5. Published microstructure studies on $\gamma\text{-Fe}_2\text{O}_3$

<u>Author</u>	<u>Crystalline Nature</u>	<u>Long Axis Direction</u>
Osmond ²²	compose of small crystallites	$\langle 111 \rangle$
Campbell ²³		any low order directions (e.g. $\langle 111 \rangle, \langle 211 \rangle, \langle 221 \rangle$ etc.)
Hurt <u>et. al.</u> ²⁴	polycrystalline	$\langle 110 \rangle$ in single crystals
Gustard and Vriend ²⁵		$\langle 110 \rangle$ (40% by volume)
Van Oosterhout ²⁶		$\langle 110 \rangle$ only
Bate ²⁷		depends on preparation conditions

Table 6. Orientation relationship between oxides

αFeOOH {100} [001]	<u>heating</u> \rightarrow	$\alpha\text{Fe}_2\text{O}_3$ {0001} [1010]	<u>reduction</u> \rightarrow	Fe_3O_4 {111} [110]	<u>Oxidation</u> \rightarrow	$\gamma\text{Fe}_2\text{O}_3$ {111} [110]
γFeOOH {100} [001]	<u>heating</u> \rightarrow	$\gamma\text{Fe}_2\text{O}_3$	<u>reduction</u> \rightarrow	Fe_3O_4	<u>Oxidation</u> \rightarrow	$\gamma\text{Fe}_2\text{O}_3$ {111} [110]

This report was done with support from the Department of Energy. Any conclusions or opinions expressed in this report represent solely those of the author(s) and not necessarily those of The Regents of the University of California, the Lawrence Berkeley Laboratory or the Department of Energy.

Reference to a company or product name does not imply approval or recommendation of the product by the University of California or the U.S. Department of Energy to the exclusion of others that may be suitable.

*LAWRENCE BERKELEY LABORATORY
TECHNICAL INFORMATION DEPARTMENT
UNIVERSITY OF CALIFORNIA
BERKELEY, CALIFORNIA 94720*